Supplementary Material

Non-TiO2-based photoanodes for photoelectrocatalytic wastewater treatment: electrode synthesis, evaluation, and characterization

Jingyang Liu[a, b, c], Huizhong Wu[a, b, c], Jiangli Sun[a, b, c], Shuaishuai Li[a, b, c]

Aydin Hassani [d, e], Minghua Zhou[a, b, c*]

[a] Key Laboratory of Pollution Process and Environmental Criteria, Ministry of Education, College of Environmental Science and Engineering, Nankai University, Tianjin 300350, China

[b] Tianjin Key Laboratory of Environmental Technology for Complex Trans-Media Pollution, College of Environmental Science and Engineering, Nankai University, Tianjin 300350, China

[c] Tianjin Advanced Water Treatment Technology International Joint Research Center, College of Environmental Science and Engineering, Nankai University, Tianjin 300350, China

[d] Department of Materials Science and Nanotechnology Engineering, Faculty of Engineering, Near East University, 99138 Nicosia, TRNC, Mersin, 10, Turkey

[e] Research Center for Science, Technology and Engineering (BILTEM), Near East University, 99138 Nicosia, TRNC, Mersin 10, Turkey

---

[*] Corresponding author.
E-mail address: zhoumh@nankai.edu.cn (M. Zhou)

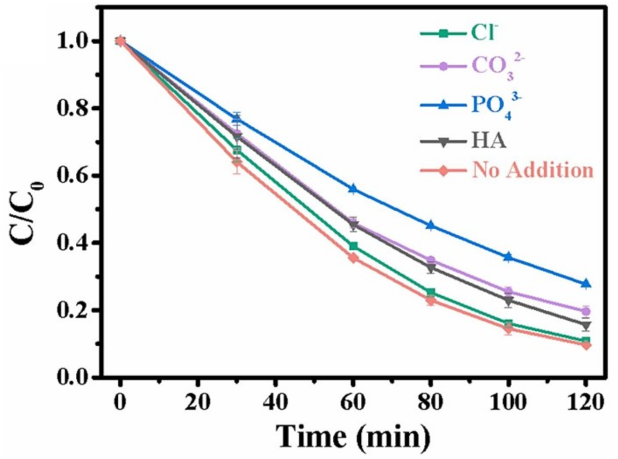

Fig. S1. The effect of co-existing anions on the degradation of sulfamethazine, reprinted from ref. 1, Copyright (2023), with permission from Elsevier.

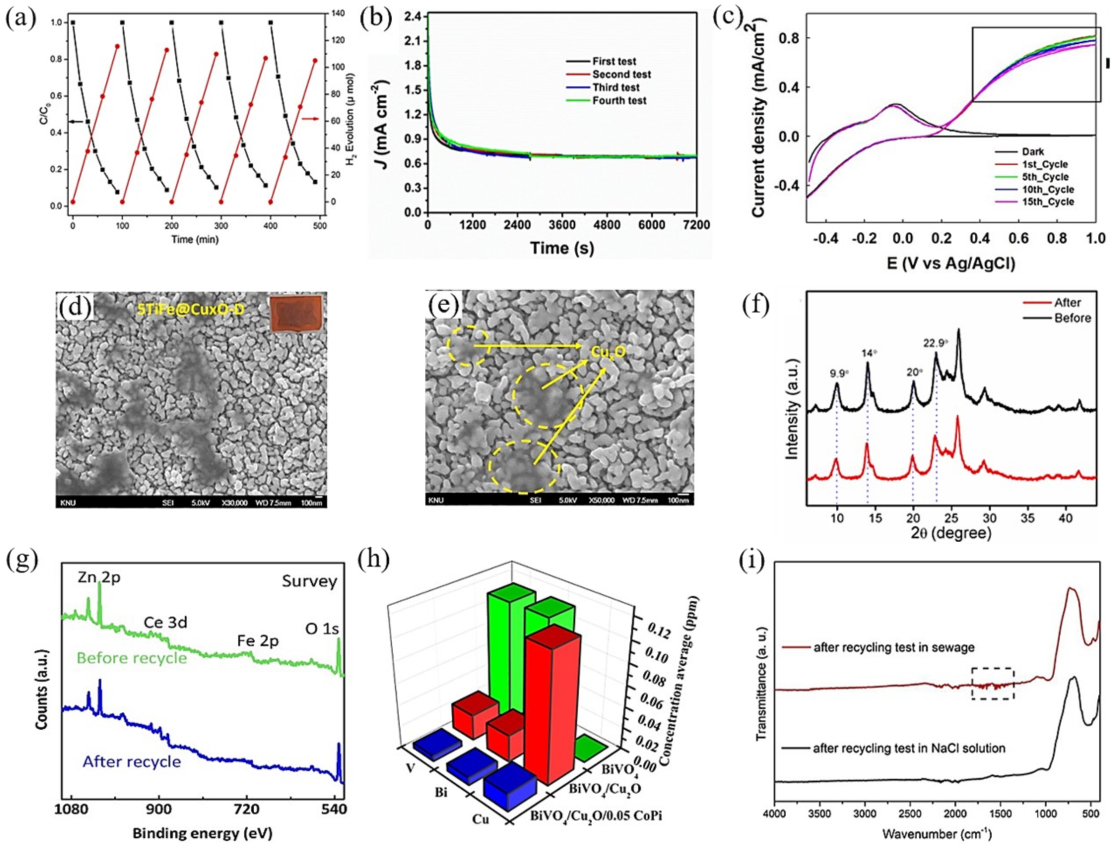

Fig. S2. Evaluation and characterization methods used for describing the stability of photoanodes. (a) The degradation efficiency of pollutants, reprinted from ref. 2, Copyright (2021), with permission from Elsevier. **Electrochemical methods:** (b) Current-time curves and (c) CV curves. (b) is reprinted from ref. 3, Copyright (2020), with permission from Elsevier. (c) is reprinted from ref. 4, Copyright (2019) American Chemical Society. **Electron microscopes:** (d-e) SEM images, reprinted from ref. 5, Copyright (2021), with permission from Elsevier. **Spectra:** (f) XRD spectra, (g) XPS spectra, (h) ICP-OES, and (i) FTIR spectra. (f) is reprinted from ref. 6, Copyright (2019), with permission from Elsevier. (g) is reprinted from ref. 7, Copyright (2020), with permission from Elsevier. (h-i) are reprinted from ref. 8 and 9, Copyright (2021), with permission from Elsevier.

The most common method to evaluate the stability of photoanodes is to test their removal efficiency after multiple cycles, and sometimes it is combined with other indicators for multifunctional photoanodes. For instance, in **Fig. S2**a, the removal of benzophenone-3 and the production of H_2 were tested simultaneously in cycling experiments, and the BL-$BiVO_4$ photoanode showed great stability after 5 cycles.[2] Besides, some electrochemical methods can help to characterize the stability of photoanodes. For example, there was almost no change after four cycles in the current-time curve of the F-$BiVO_4$@NiFe-LDH photoanode (**Fig. S2**b[3]); in **Fig. S2**c, the photocurrent of the WO_3 photoanode decreases with the increase of CV cycles when bias potentials exceed 0.5 V, which is caused by the instability of the photoanode at high potential.[4] With the help of SEM, Cu_xO could still be observed on the surface of the hematite structures after repeated use of 5TiFe@Cu_xO-D (**Fig. S2**d-e[5]). In addition, the change in components can be observed through many kinds of spectra: the position and intensity of the peaks of the XRD image of the SA-PDI film shown in **Fig. S2**f did not change significantly after use;[6] after repeated degradation experiments of TC, the change in XPS spectra of the Ce@Fe-2 photoanode was not obvious (**Fig. S2**g[7]); the dissolution of metal is inversely proportional to the stability of the electrode in **Fig. S2**h;[8] the FTIR spectra of the MoS_2@BL-$BiVO_4$ photoanode after recycling tests in sewage; showed some new peaks compared with those of the photoanode after use in NaCl solution (**Figure S2**i[9]).

$$IPCE = \frac{1240 \times I_p(\lambda)}{P(\lambda) \times \lambda} \tag{1}$$

$$APCE = \frac{IPCE}{1 - 10^{-A}} \tag{2}$$

$$\eta = \frac{\Delta G^0 \times R}{P} \tag{3}$$

$$\eta = \frac{(E - V_{app}) \times I}{P} \tag{4}$$

In **Eq. S1**, λ is the wavelength of incident light (nm), I_p (λ) and P(λ) are the photocurrent density (A/m^2) and incident power density of light (W/m^2) at the wavelength of λ, respectively. In **Eq. S2**, A is the absorbance of light. In **Eq. S3**, ΔG^0 and R are the standard Gibbs energy (kJ/mol) for the photodegradable substance and the rate of production (mol/s), respectively, and P is the incident radiation power (W/m^2). In **Eq. S4**, E is the standard potential for the photodegradable substance (V), V_{app} is the applied bias (V), and I is the current density (A/m^2) involved in the decomposition process.

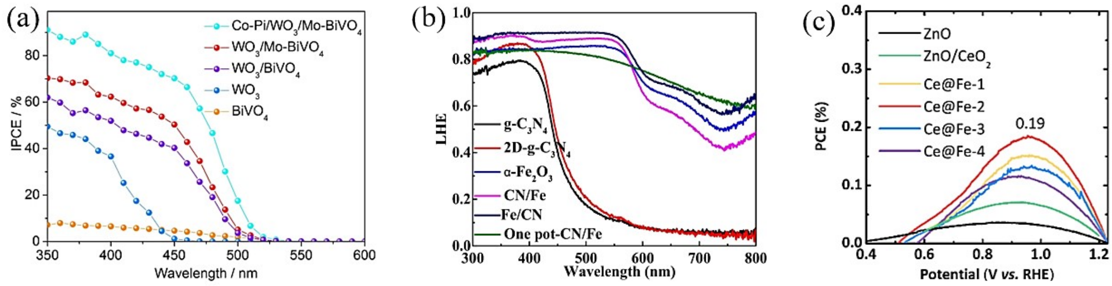

Fig. S3. Characterization techniques for evaluating light utilization efficiency. (a) IPCE curves of different photoanodes implemented at 1.23 V vs. RHE, reprinted from ref. 10, Copyright (2017), with permission from Elsevier. (b) LHE curves of different photoanodes, reprinted from ref. 11, Copyright (2022), with permission from Elsevier. (c) PCE curves of ZnO, ZnO/CeO$_2$, and Ce@Fe samples, reprinted from ref. 7, Copyright (2020), with permission from Elsevier.

Incident photon-to-current efficiency (IPCE), also known as external quantum efficiency (EQE), is the most common indicator used to evaluate light utilization efficiency. IPCE can be calculated by **Eq. S1**.[12] As shown in **Fig. S3**a, after the construction of the $WO_3/BiVO_4$ heterostructure, not only was the response range expanded, but the IPCE value was also improved. Among them, Co-Pi/WO_3/Mo-$BiVO_4$ exhibited the best IPCE value, which was due to the improvement of charge separation efficiency.[10] Unlike EQE, internal quantum efficiency (IQE), also known as absorbed photon to current conversion efficiency (APCE), is the ratio of the number of charge carriers generated by the photoanode to the number of photons it absorbs.[13] The relationship between them can be described as **Eq. S2**. In, **Eq. S2**, the denominator ($1-10^{-A}$) is defined as light harvesting efficiency (LHE),[14] which can be used to evaluate the light absorption performance of photoanodes. As shown in **Fig. S3**b, the Fe/CN photoanode exhibited enhanced light absorption, which was attributed to the heterojunction of 2D-g-C_3N_4 and α-Fe_2O_3. Studies have shown that LHE can be improved by increasing the light scattering efficiency, such as improving the reflection of photons in the photoanodes.[15]

Moreover, light utilization efficiency can be calculated from a thermodynamic point of view. For instance, η is calculated by **Eq. S3**. When the degree of photodegradable substance and applied bias are considered, it can also be calculated by **Eq. S4** (assuming the Faradaic conversion efficiency is 100%).[13] When it comes to water splitting to produce hydrogen, $E = 1.23$ V, and in this case, η is also called applied bias photon-to-current efficiency (ABPE). ABPE is also an indicator for evaluating the light utilization efficiency of non-TiO_2-based photoanodes used for wastewater treatment.[11, 16] For instance, in the study by He et al., this indicator, which has the same form as ABPE, was called “PCE,” and the PCE curves of ZnO, ZnO/CeO_2, and Ce@Fe samples were tested. Ce@Fe-2 obtained the highest PCE performance of 0.19% (**Fig. S3**c), which confirmed that the light harvest of photoanodes can be improved and the recombination of holes and electrons can be inhibited by coupling CeO_2 and α-Fe_2O_3.[7] Finally, solar-to-hydrogen (STH) efficiency is sometimes considered when simultaneous pollutant degradation and H_2 generation are involved.[17]

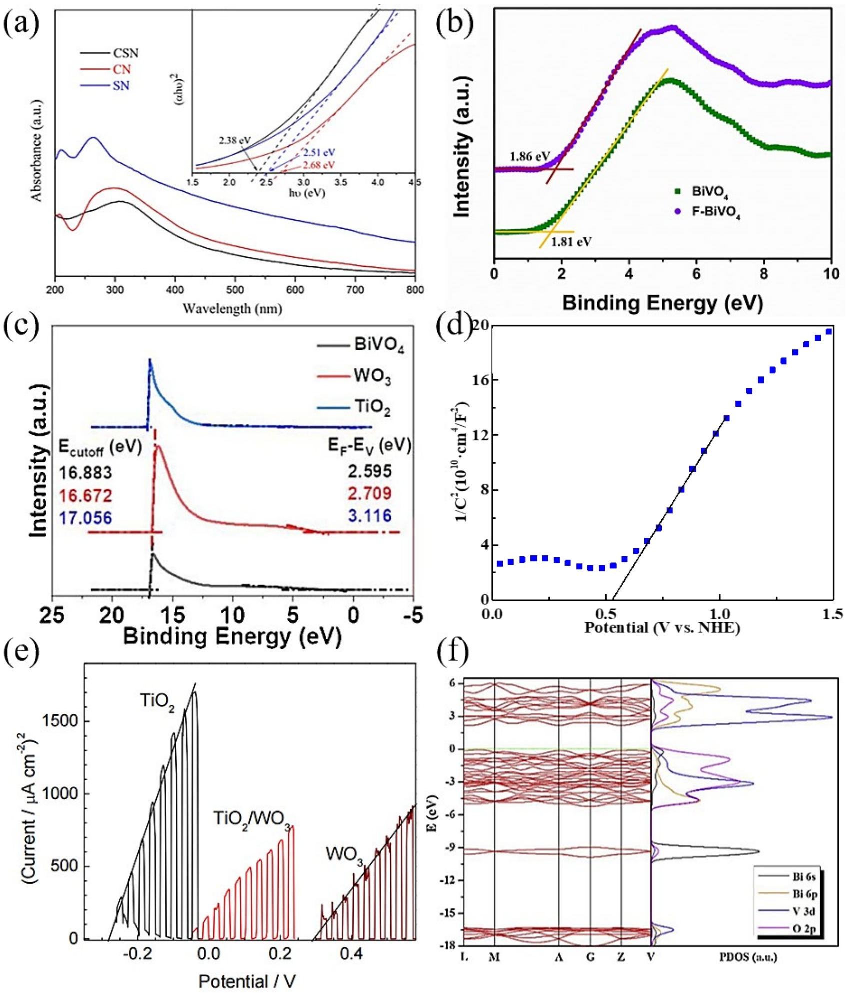

Fig. S4. Methods to calculate the E_g of photoanodes. (a) UV-vis DRS of three photoanodes (inside is the Tauc plot), reprinted from ref. 18, Copyright (2022), with permission from Elsevier. (b) Relative VB positions of $BiVO_4$ and F-$BiVO_4$ from VB-XPS, reprinted from ref. 3, Copyright (2020), with permission from Elsevier. (c) UPS spectra of $BiVO_4$, WO_3, and TiO_2 photoanodes, reprinted from ref. 19, Copyright (2021), with permission from Elsevier. (d) Mott-Schottky plots of α-Fe_2O_3, reprinted from ref. 11, Copyright (2022), with permission from Elsevier. (e) The square of current density with applied potential of TiO_2, WO_3, and TiO_2/WO_3, reprinted from ref. 20, Copyright (2015), with permission from Elsevier. (f) Calculated energy band structure and corresponding density of states of the $BiVO_4$ photoanode, reprinted from ref. 21, Copyright (2019), with permission from Elsevier.

To obtain the optical bandgap of semiconductors directly, UV-vis DRS is the most popular technique. The classical UV-vis DRS spectra are presented in **Fig. S4**a, showing the absorbance of the photoanode as a function of incident light wavelength. Bandgap information can be roughly estimated from the absorption edges of UV-Vis DRS by applying the following relationship:[22]

$$E_g = \frac{1240}{\lambda_g} \tag{5}$$

where λ_g is the band-edge wavelength. The most frequently used method is the Tauc relationship,[23] which can be described as:

$$\alpha h\nu = A(h\nu - E_g)^{n/2} \tag{6}$$

where α is the absorption coefficient, $h\nu$ is the photon energy, and A is a constant. The value of n depends on the type of semiconductor; it takes values of 1 and 4 for direct transition bandgap and indirect transition bandgap, respectively. According to that, the Tauc plot takes $(\alpha h\nu)^{2/n}$ as the vertical axis and $h\nu$ as the horizontal axis, and E_g can be calculated from the intercept of the prolonged line of the linear part in the Tauc plot (the inset figure of **Figure S4**a). Some researchers[8] use absorbance to approximate the absorption coefficient since absorbance is proportional to the absorption coefficient according to the Beer-Lambert Law,[24] the results of bandgap energy won't change after the substitution of α with absorbance. Others consider the influence of scattering and use $F(R_\infty)$ in the Kubelka Munk function (**Eq. S7**) to approximate α.[21, 25]

$$F(R_\infty) = \frac{(1 - R_\infty)^2}{2R_\infty} = \frac{\alpha}{s} \tag{7}$$

where R_∞ represents the limit value of the reflection coefficient R of an infinitely thick sample, α and s are the absorption coefficient and scattering coefficient, respectively.

Apart from obtaining the bandgap energy directly, it can also be determined after determining the conduction band minimum (CBM) edge and valence band maximum (VBM) edge positions. VB-XPS is usually used to characterize the VB position, as shown in **Fig. S4**b. The relative valence band positions of $BiVO_4$ and F-$BiVO_4$ photoanodes can be obtained from high-resolution VB-XPS spectra; the results can be transferred by:

$$E_{NHE}/V = \Phi + E_{VB-XPS} - 4.44 \tag{8}$$

where E_{NHE}/V is the standard electrode potential, Φ is the electron work function of the analyzer.[26, 27] Ultraviolet photoelectron spectroscopy (UPS) can also be used to determine the VB position. Li et al.[19] compared the PEC production of active chlorine radicals by WO_3, TiO_2, and $BiVO_4$ photoanodes, and the VBM of the three photoanodes was calculated with the help of UPS (**Fig. S4**c). VBM can be calculated by the following equation:

$$VBM = hv - E_{cutoff} + E_{Fermi} \tag{9}$$

where hv is 21.22 eV (He-I line with photon energy of 21.22 eV), E_{cutoff} and E_{Fermi} are the binding energies of the secondary electron cutoff edge and Fermi edge (the difference between the Fermi level and valence-band maximum). The results are presented with electron energy in the vacuum, and it can be transferred to normal hydrogen potential with the help of an equation in the form of **Eq. S8**.[28]

CBM or VBM can also be determined from the flat band potential. It can be determined from the Mott-Schottky equation:[29, 30]

$$\frac{1}{C^2}=\frac{2}{\varepsilon\varepsilon_0 A^2 e N_D}\left(E-E_{fb}-\frac{k_BT}{e}\right)\ for\ n-type \tag{10}$$

$$\frac{1}{C^2}=\frac{2}{\varepsilon\varepsilon_0 A^2 e N_A}\left(-E+E_{fb}-\frac{k_BT}{e}\right)\ for\ p-type \tag{11}$$

where C is the space charge capacitance, A is the electrode surface area, N_D and N_A are the donor density and acceptor density, respectively, e is the electronic charge, T is the absolute temperature, ε and ε_0 are the dielectric constant of the catalyst and vacuum dielectric constant, respectively, k_B is Boltzmann's constant, E is the applied voltage, E_{fb} is the flat band potential. After taking C^{-2} and V as the vertical and horizontal axes, respectively, the intercept on the V axis represents $V_{fb}+\frac{k_BT}{e}$ for n-type semiconductors and $V_{fb}-\frac{k_BT}{e}$ for p-type semiconductors, and the flat band potential can be determined (**Fig. S4**d).

Moreover, the relationship between photocurrent and applied potential can also help determine the flat band potential according to the Butler-Wilson theory:[31]

$$E-E_{fb}\sim(J/\alpha W_0 e\varphi_0)^2 \tag{12}$$

where J, W_0, and φ_0 represent photocurrent, the depletion layer width for a potential of 1 V across it, and the photon flux, respectively. According to this, the square of the photocurrent should linearly increase with the applied potential, and the semiconductor E_{fb} can be estimated from extrapolation (**Fig. S4**e). Later, the energy difference between CBM/VBM and the flat band potential is assumed to be about 0.2 eV.[32, 33]

Zhang et al.[11] used Mott-Schottky plots to estimate the CB position (**Fig. S4**d), and VB-XPS to determine the VB position. E_g is consistent with results from UV-vis DRS. Oliveira et al.[20] used **Eq. S12** to calculate the flat band potential of TiO_2, WO_3, and TiO_2/WO_3 photoanodes (**Fig. S4**e). The calculated results were combined with the E_g to determine the VBM position and compared with molecular orbital energies for organic pollutant molecules.

Apart from experimental methods, theoretical calculations can also help to obtain E_g and the adsorption coefficient. Especially, DFT calculations have been widely used to learn about the electronic structure of non-TiO_2-based photoanodes in combination with experimental characterizations. For instance, to learn more about $BiVO_4$, Li et al.[21] carried out DFT calculations using the Perdew-Burke-Ernzerhof (PBE) version of the generalized gradient approximation (GGA). As illustrated in **Fig. S4**f, the energy band structure of $BiVO_4$ indicates that it has a minimum indirect energy bandgap of 2.23 eV, which is nearly approaching the result of 2.45 eV obtained from the Tauc plot. Although there are differences between the values of the two methods, which may be ascribed to the typical restrictions of DFT calculations, DFT can reveal the occupied orbitals of the VBM and CBM according to the density of states (DOS) of the semiconductors; it can also help to distinguish the type of semiconductors (direct bandgap or indirect bandgap). Similarly, Sharp and coworkers[34] characterized the electronic structure of monoclinic $BiVO_4$ (**Fig. S5a**) with the help of a combination of DFT calculations and experimental methods. Moreover, Bahers et al.[35] compared the mean absolute error of four investigated functionals on the bandgap and other properties of many semiconductors (**Fig. S5b**), and they found that the HSE06 functional always obtained the best agreement compared to experiments. Bahers and Takanabe[17] systematically studied theoretical and experimental characterizations of the bandgap and other properties of the semiconductors. They concluded new functionals for semiconductor property calculations with lower errors, and some limitations and corresponding solving methods were proposed; detailed information can be found in their review.

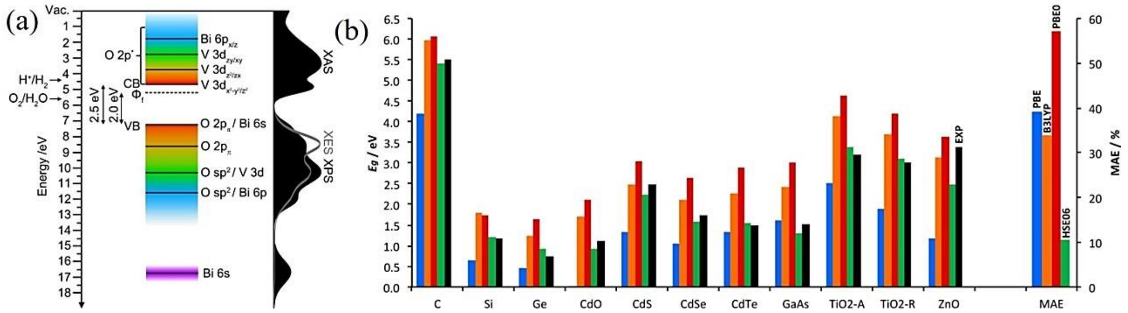

Fig. S5. (a) Energy level diagram of monoclinic scheelite $BiVO_4$ according to DFT calculations and experimental data, reprinted with permission from ref. 34, Copyright (2014) American Chemical Society. (b) Comparison of the bandgap calculated by four different methods with experimental data and mean absolute error. reprinted with permission from ref. 35, Copyright (2014) American Chemical Society.

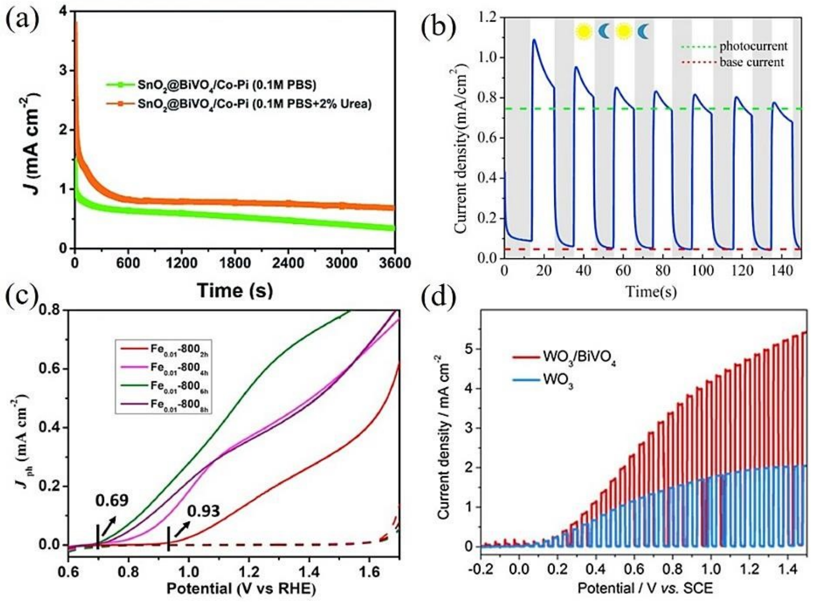

Fig. S6. (a) Photocurrent-time response curves of $SnO_2@BiVO_4/Co-Pi$ photoanode under different electrolytes, reprinted with permission from ref. 36, Copyright (2019) Royal Society of Chemistry. (b) Transient current responses to the ON-OFF illumination cycle on the α-Fe_2O_3-based photobioanode, reprinted from ref. 37, Copyright (2016), with permission from Elsevier. (c) LSV curves of α-Fe_2O_3 photoanodes at different hydrothermal treatment times, reprinted from ref. 5, Copyright (2021), with permission from Elsevier. (d) Chopped LSV curves of the WO_3 and $WO_3/BiVO_4$ photoanodes, reprinted from ref. 38, Copyright (2018), with permission from Elsevier.

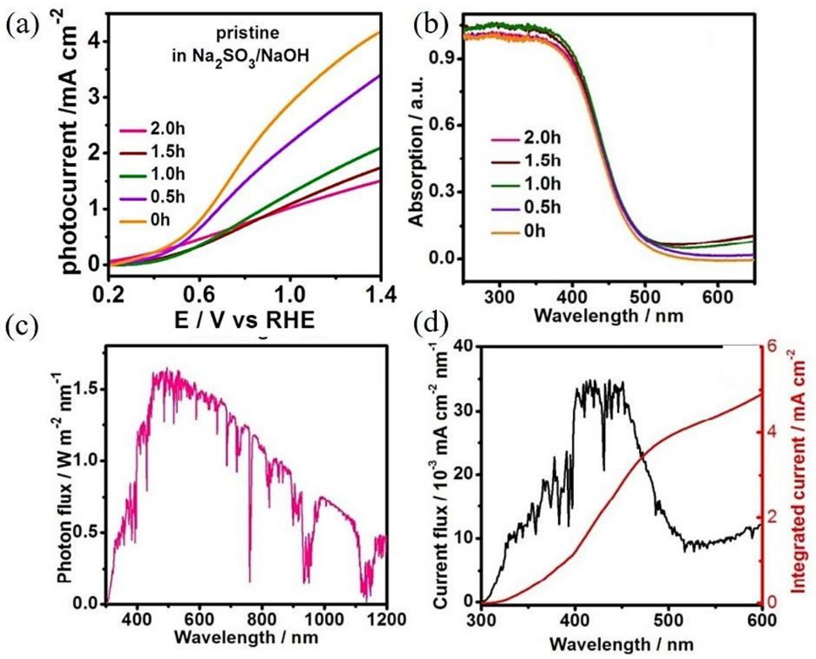

Fig. S7. (a) Photocurrent of GaN:ZnO photoanodes with different moisture exposure times in 1 M NaOH and 0.5 M Na_2SO_3 mixed aqueous solution. (b) The absorption spectra for GaN:ZnO. (c) The spectrum of AM 1.5G sunlight. (d) The current flux calculated based on its light absorption and the integrated current assuming 100% IPCE, reprinted with permission from ref. 39, Copyright (2017) American Chemical Society.

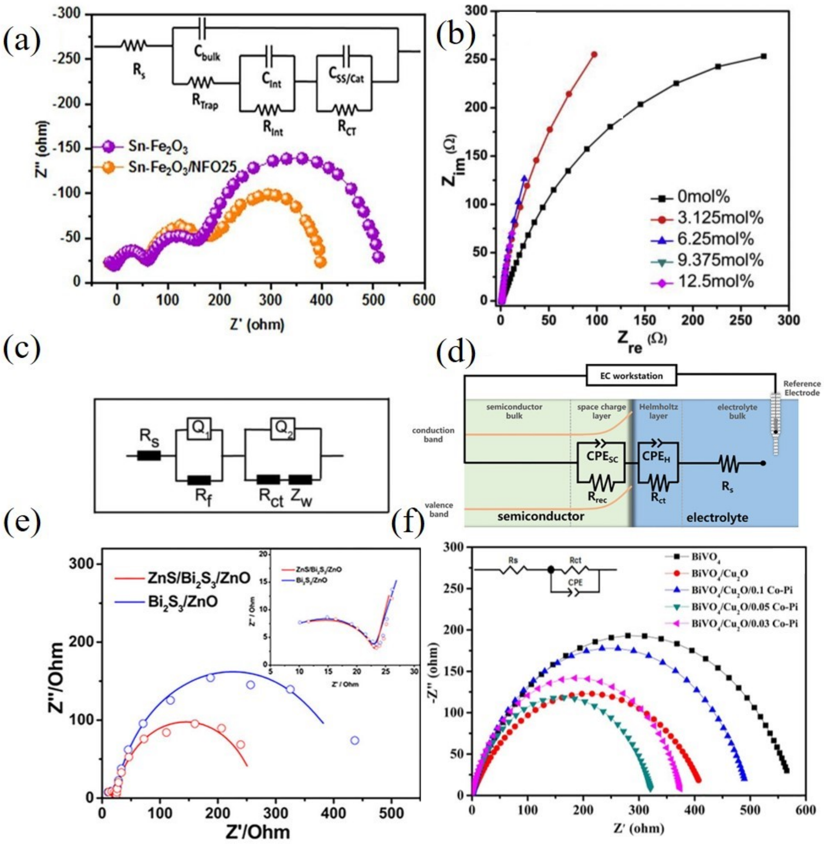

Fig. S8. (a) Nyquist plots of bare Sn-Fe_2O_3 and Sn-Fe_2O_3/NFO25 photoanodes at 1.23 V under illumination (inset is its equivalent circuit), reprinted from ref. 40, Copyright (2021), with permission from Elsevier. (b) Nyquist plots of $Ir_xZn_{1-x}O$/Ti electrodes with different Ir contents under UV irradiation and (c) the corresponding electrical equivalent circuit, reprinted from ref. 41, Copyright (2020), with permission from Elsevier. (d) Equivalent circuit for the PEC process of Bi_2S_3/ZnO NRA and ZnS/Bi_2S_3/ZnO NRA and (e) the corresponding Nyquist plots, reprinted with permission from ref. 42, Copyright (2017) American Chemical Society. (e) Nyquist plots of different photoanodes, and the inset shows the equivalent circuit, reprinted from ref 8, Copyright (2021), with permission from Elsevier.

Reference

1 H. Wu, Z. Hu, R. Liang, O.V. Nkwachukwu, O.A. Arotiba and M. Zhou, *Appl. Catal. B: Environ.*, 2023, **321**, 122053.

2 Z. Zheng, J. He, C. Dong and I.M.C. Lo, *Chem. Eng. J.*, 2021, **419**, 129418.

3 J. Liu, J. Li, Y. Li, J. Guo, S. Xu, R. Zhang and M. Shao, *Appl. Catal. B: Environ.*, 2020, **278**, 119268.

4 M.S. Koo, X. Chen, K. Cho, T. An and W. Choi, *Environ. Sci. Technol.*, 2019, **53**, 9926-9936.

5 L.R. Nagappagari, J. Lee, H. Lee, B. Jeong and K. Lee, *Environ. Pollut.*, 2021, **271**, 116318.

6 H. Miao, J. Yang, G. Peng, H. Li and Y. Zhu, *Sci. Bull.*, 2019, **64**, 896-903.

7 S. He, C. Yan, X. Chen, Z. Wang, T. Ouyang, M. Guo and Z. Liu, *Appl. Catal. B: Environ.*, 2020, **276**, 119138.

8 X. Li, J. Wan, Y. Ma, Y. Wang and X. Li, *Chem. Eng. J.*, 2021, **404**.

9 Z. Zheng and I.M.C. Lo, *Appl. Catal. B: Environ.*, 2021, **299**, 120636.

10 Q. Zeng, J. Li, L. Li, J. Bai, L. Xia and B. Zhou, *Appl. Catal. B: Environ.*, 2017, **217**, 21-29.

11 O.K. Varghese and C.A. Grimes, *Sol. Energy Mater. Sol. Cells*, 2008, **92**, 374-384.

12 P. Lianos, *J. Hazard. Mater.*, 2011, **185**, 575-590.

13 B. Lei, D. Xu, B. Wei, T. Xie, C. Xiao, W. Jin and L. Xu, *ACS Appl. Mater. Inter.*, 2021, **13**, 4785-4795.

14 R. Boppella, A. Mohammadpour, S. Illa, S. Farsinezhad, P. Basak, K. Shankar and S.V. Manorama, *Acta Mater.*, 2016, **119**, 92-103.

15 M.B. Costa, M.A. de Araújo, M.V.D.L. Tinoco, J.F.D. Brito and L.H. Mascaro, *J. Energy Chem*, 2022, **73**, 88-113.

16 L. Zhang, X. Zhang, C. Wei, F. Wang, H. Wang and Z. Bian, *Chem. Eng. J.*, 2022, **435**, 134873.

17 T. Le Bahers and K. Takanabe, *J. Photochem. Photobiol. C-Photochem. Rev.*, 2019, **40**, 212-233.

18 Z. Dai, J. Lian, Y. Sun, L. Li, H. Zhang, N. Hu and D. Ding, *Chem. Eng. J.*, 2022, **433**, 133766.

19 X. Li, M. Kan, T. Wang, Z. Qin, T. Zhang, X. Qian, Y. Kuwahara, K. Mori, H. Yamashita and Y. Zhao, *Appl. Catal. B: Environ.*, 2021, **296**, 120387.

20 H.G. Oliveira, L.H. Ferreira, R. Bertazzoli and C. Longo, *Water Res.*, 2015, **72**, 305-314.

21 F. Li, W. Zhao and D.Y.C. Leung, *Appl. Catal. B: Environ.*, 2019, **258**, 117954.

22 X. Mei, J. Bai, S. Chen, M. Zhou, P. Jiang, C. Zhou, F. Fang, Y. Zhang, J. Li, M. Long and B. Zhou, *Environ. Sci. Technol.*, 2020, **54**, 11515-11525.

23 J. Tauc, R. Grigorovici and A. Vancu, *Physica Status Solidi (B)*, 1966, **15**, 627-637.

24 *Doc. Ophthalmol.*, 1974, **38**, 279-282.

25 C. Wang, M. Sun, Y. Zhao, M. Huo, X. Wang and M. Elimelech, *Environ. Sci. Technol.*, 2021, **55**, 604-613.

26 Z. Hong, B. Shen, Y. Chen, B. Lin and B. Gao, *J. Mater. Chem. A.*, 2013, **1**, 11754-

11761.

27 J. Yuan, X. Liu, Y. Tang, Y. Zeng, L. Wang, S. Zhang, T. Cai, Y. Liu, S. Luo, Y. Pei and C. Liu, *Appl. Catal. B: Environ.*, 2018, **237**, 24-31.

28 R.M. Fernández-Domene, R. Sánchez-Tovar, B. Lucas-granados, M.J. Muñoz-Portero and J. García-Antón, *Chem. Eng. J.*, 2018, **350**, 1114-1124.

29 K. Gelderman, L. Lee and S.W. Donne, *J. Chem. Educ.*, 2007, **84**, 685.

30 M. Li, W. Wu, K. Liu, G. Hu and H. Xu, *Electrochim. Acta*, 2012, **71**, 100-105.

31 M.A. Butler, *J. Appl. Phys.*, 1977, **48**, 1914-1920.

32 Y. Matsumoto, *J. Solid State Chem.*, 1996, **126**, 227-234.

33 K. Cheng, Y. Wu and Y. Hu, *Mater. Res. Bull.*, 2013, **48**, 2457-2468.

34 J.K. Cooper, S. Gul, F.M. Toma, L. Chen, P. Glans, J. Guo, J.W. Ager, J. Yano and I.D. Sharp, *Chem. Mater.*, 2014, **26**, 5365-5373.

35 T. Le Bahers, M.R.E. Rat and P. Sautet, *J. Phys. Chem. C.*, 2014, **118**, 5997-6008.

36 J. Liu, J. Li, M. Shao and M. Wei, *J. Mater Chem. A.*, 2019, **7**, 6327-6336.

37 H. Feng, Y. Liang, K. Guo, N. Li, D. Shen, Y. Cong, Y. Zhou, Y. Wang, M. Wang and Y. Long, *Water Res.*, 2016, **102**, 428-435.

38 Q. Zeng, L. Lyu, Y. Gao, S. Chang and C. Hu, *Appl. Catal. B: Environ.*, 2018, **238**, 309-317.

39 Z. Wang, X. Zong, Y. Gao, J. Han, Z. Xu, Z. Li, C. Ding, S. Wang and C. Li, *ACS Appl Mater. Inter.*, 2017, **9**, 30696-30702.

40 S. Seenivasan, S. Adhikari and D. Kim, *Chem. Eng. J.*, 2021, **422**.

41 K. Feng, Y. Lin, J. Guo, Z. Ye, Y. Zhang, Q. Ma, Y. Shao, K. Chen, J. Zhuang, D. Lin and T. Lin, *J. Hazard. Mater.*, 2020, **393**, 122488.

42 Y. Lu, R. Popescu, D. Gerthsen, Y. Feng, W. Su, Y. Hsu and Y. Chen, *ACS Appl. Mater. Inter.*, 2022, **14**, 7756-7767.